

Accepted Article Preview: Published ahead of advance online publication



Off-Axis Bright- and Dark-Field OCT for Non-destructive Subsurface Defect Detection in Silicon Carbide

Dacheng Wang, Chengchen Zhou, Yukun Wang, Lingzhong Li, Yue Ding, Zhongkai Liu, Nanguang Chen, Linbo Liu, Xiaokun Wang, Donglin Xue and Xuejun Zhang

Cite this article as: Dacheng Wang, Chengchen Zhou, Yukun Wang, Lingzhong Li, Yue Ding, Zhongkai Liu, Nanguang Chen, Linbo Liu, Xiaokun Wang, Donglin Xue, Xuejun Zhang. Off-Axis Bright- and Dark-Field OCT for Non-destructive Subsurface Defect Detection in Silicon Carbide. *Light: Advanced Manufacturing* accepted article preview 08 April, 2026; doi: 10.37188/lam.2026.060

This is a PDF file of an unedited peer-reviewed manuscript that has been accepted for publication. LAM are providing this early version of the manuscript as a service to our customers. The manuscript will undergo copyediting, typesetting and a proof review before it is published in its final form. Please note that during the production process errors may be discovered which could affect the content, and all legal disclaimers apply.

Received 13 January 2026; revised 7 April 2026; accepted 8 April 2026;
Accepted article preview online 08 April 2026

Off-Axis Bright- and Dark-Field OCT for Non-destructive Subsurface Defect Detection in Silicon Carbide

Dacheng Wang^{1,2,3}, Chengchen Zhou^{1,2,3}, Yukun Wang^{1,3*}, Lingzhong Li^{1,3}, Yue Ding^{1,3},
Zhongkai Liu^{1,3}, Nanguang Chen⁴, Linbo Liu⁵, Xiaokun Wang^{1,3}, Donglin Xue^{1,3}, Xuejun
Zhang^{1,3}

¹*Changchun Institute of Optics, Fine Mechanics and Physics, Chinese Academy of Sciences,
Changchun, 130033, Jilin, China*

²*University of Chinese Academy of Sciences, 100049, Beijing, China*

³*State Key Laboratory of Advanced Manufacturing for Optical Systems, Changchun, 130033,
Jilin, China*

⁴*National University of Singapore, Department of Biomedical Engineering, Singapore.*

⁵*Guangzhou National Laboratory, Guangzhou International Bio Island, Guangzhou, China.*

Abstract

The exceptional mechanical and thermal properties of silicon carbide (SiC) make it vital for advanced optics; however, its hardness and brittleness cause subsurface defects (SSDs) during machining that impair performance and longevity. Current detection methods remain destructive and inefficient, whereas conventional optical coherence tomography (OCT) struggles with limited penetration, surface scattering interference, and poor defect contrast in this highly scattering material. We propose a non-destructive off-axis bright- and dark-field synchronous OCT (BADF-OCT) method that captures complementary scattered signals at dual angles to enhance weak subsurface feature detection. The broadband 1100–1500 nm near-infrared spectral-domain OCT system provides high axial resolution with adequate SiC penetration. Experimental validation on reaction-bonded SiC demonstrates clear discrimination between surface fracture and subsurface crack layers, providing reliable detection of micrometre-scale defects at depths up to ~200 μm . Three-dimensional volumetric imaging combined with bright/dark-field data fusion effectively distinguishes true SSDs from surface contaminants, significantly improving the recognition accuracy. This study is expected to contribute to the development of high-energy lasers, large-scale scientific facilities for light sources, and advanced optical manufacturing.

Keywords: Optical Coherence Tomography; Silicon Carbide; Subsurface Defects; Bright and Dark Field; Non-destructive Testing

1. Introduction

Silicon carbide (SiC) has emerged as a key structural and functional material for advanced optical systems, particularly in large-aperture space mirrors¹, high-power laser optics², and extreme-environment optical instruments³. Owing to its outstanding properties, including a high stiffness-to-weight ratio, excellent thermal stability, a low coefficient of thermal expansion, high hardness, and superior wear and corrosion resistance, SiC offers significant

39 advantages over traditional optical materials such as glass ceramics and single-crystal silicon.
40 These characteristics make SiC particularly attractive for applications requiring a lightweight
41 design, high-dimensional stability, and long-term environmental robustness. Despite these
42 advantages, the extreme hardness and low fracture toughness of SiC pose substantial
43 challenges during precision machining processes such as grinding and polishing^{4,5}.
44 Mechanical material removal inevitably introduces subsurface defects (SSDs), including
45 micro-cracks, median and lateral cracks, and fractured grain boundaries beneath the surface⁶⁻⁸.
46 Such SSDs are often distributed over tens to hundreds of micrometres in depth and cannot be
47 fully eliminated by the subsequent polishing steps without excessive material removal. If left
48 undetected, SSDs can degrade the optical performance, reduce the mechanical strength, and
49 compromise the long-term reliability of SiC optical components. Therefore, the accurate
50 characterisation and control of SSDs are essential for improving the manufacturing yield and
51 ensuring component performance.

52 The precise detection of defect information is a prerequisite for eliminating or suppressing
53 SSDs. Existing SSD detection methods can be categorised into destructive and
54 non-destructive techniques, based on whether they cause damage to the test specimen.
55 Destructive methods involve the partial or complete destruction of the specimen to expose the
56 defect location, followed by obtaining results through appropriate microscopic observations.
57 Representative processing methods include chemical etching, cross-sectional microscopy^{9,10},
58 and angle polishing¹¹. These methods are simple and highly intuitive, and yield reliable
59 experimental results. However, they are only suitable for comparative experiments. In
60 component manufacturing inspections, both the machine and test piece must be processed
61 from the same batch, resulting in extremely high inspection costs. To align with the
62 manufacturing process, the inspection workflow becomes extremely cumbersome. In contrast,
63 non-destructive testing methods utilise the differences in how internal defects within materials
64 respond to light, sound, or electrical signals to detect anomalies and flaws within the
65 material^{12,13}. X-rays can undergo diffraction with crystal lattices, enabling the calculation of
66 comprehensive stresses within a certain sample depth based on the positions of the diffraction
67 fringes. However, the measurement results vary significantly among the different X-ray
68 types¹⁴. Laser confocal scanning microscopy uses the confocal optical path characteristics to
69 perform point measurements based solely on sample information within the focal plane. By
70 moving the sample in three dimensions, this method enables the detection of scattered signals
71 from defects at different depths within the optical components and provides depth information
72 for SSDs^{15,16}. Fluorescence confocal microscopy utilises the fluorescence effect of fluorescent
73 media penetrating the SSDs in optical components under laser illumination to achieve SSD
74 detection¹⁷⁻¹⁹. Kurniawan employed confocal subsurface photoluminescence
75 spectro-microscopy to identify subsurface, electrically active screw dislocations in SiC in a
76 non-destructive manner, achieving detection depths of up to 100 μm . However, this method is
77 largely ineffective for detecting non-electrically active or pure edge dislocations²⁰. The
78 greatest advantage of this technology is its non-destructive nature, which enables the
79 monitoring and research of SSD changes throughout the manufacturing process. However,
80 such methods typically require high-specification experimental equipment and environments.
81 In addition, their relatively low detection efficiency makes them unsuitable for rapid SSD
82 inspection in large-aperture optical components. Although total internal reflection microscopy

83 is available, its effectiveness is severely limited for non-transparent samples. Furthermore,
84 owing to the high density of SiC, existing methods can only penetrate several nanometres or
85 micrometres. Therefore, they are suitable only for detecting SSDs in thin SiC wafers, as they
86 fail to observe deeper structural damage.

87 As a high-resolution, non-destructive, and non-invasive optical imaging technique, optical
88 coherence tomography (OCT) has been applied extensively in the biomedical and industrial
89 inspection fields. Its convenient and efficient testing process, coupled with its clear and
90 intuitive imaging results, represent the prominent advantages of this technology for practical
91 applications²¹⁻²⁷. The high timeliness and flexibility of OCT enable it to deliver outstanding
92 advantages in industrial in situ detection, such as three-dimensional (3D) printing in situ
93 measurements and laser grooving monitoring^{28,29}. Hu measured the SSDs in components
94 using polarisation-sensitive OCT and estimated the morphology of their defects, but did not
95 test SiC³⁰. Israelsen constructed the first mid-infrared OCT system and applied it to real-time
96 non-destructive testing³¹. At present, OCT technology faces the following challenges in
97 industrial applications: (1) Poor environmental adaptability: Industrial vibrations and
98 temperature fluctuations increase the image noise, compromising the detection accuracy and
99 signal-to-noise ratio (SNR). (2) Difficulty balancing detection efficiency, resolution, and
100 accuracy: High-resolution scanning reduces the detection efficiency, whereas device response
101 deviations under high-frequency operation cause information loss, failing to meet production
102 line demands for efficient and precise inspection. (3) Existing OCT technology faces
103 limitations in inspecting samples with low surface roughness. Noise interference caused by
104 strong surface reflections reduces or even obscures the contrast in deep-layer structure
105 imaging. These issues constrain the widespread industrial adoption of OCT and require
106 solutions through system design, algorithm optimisation, and hardware upgrades³².

107 To overcome the limitations of conventional OCT, including its strong surface scattering
108 interference, limited spectral resolution, and high false-negative rates associated with
109 single-mode imaging, off-axis OCT configurations have been introduced to enhance the
110 collection of multiply-scattered photons and suppress specular reflections^{33,34}. Building upon
111 this concept, this study proposes an off-axis bright- and dark-field synchronous OCT
112 (BADF-OCT) architecture for non-destructive SSD detection in SiC. The proposed system
113 captures complementary defect information that is inaccessible to single-channel OCT by
114 simultaneously acquiring scattered signals from two angular channels, thereby significantly
115 improving the detection robustness. A broadband near-infrared spectral-domain OCT system
116 operating in the 1100–1500 nm range is specifically designed to achieve both high axial
117 resolution and large penetration depth in SiC. Combined with a dual-channel fibre array
118 spectrometer, this system enables synchronous bright- and dark-field detection and 3D
119 volumetric imaging. The availability of 3D data further enhances the defect recognition
120 accuracy by enabling reliable discrimination between true SSD and surface-related artefacts.
121 The principles of bright-/dark-field interference, data acquisition, processing, and defect
122 identification were analysed, and the experimental results on reaction-bonded SiC samples
123 validated the effectiveness of the proposed approach. The results demonstrate that the
124 BADF-OCT system provides a practical and reliable non-destructive solution for SSD
125 inspection and quality control in SiC optical component manufacturing.

126 **2. Principle and Method**127 **2.1 Principle of Off-Axis Bright- and Dark-Field OCT**

128 The Fourier-domain OCT system employs low-coherence interferometry for tomographic
 129 imaging, with its optical path structure based on the Michelson interferometer. Off-axis
 130 bright- and dark-field imaging involves illuminating the sample using an off-axis light source.
 131 The photons reach the sample surface and interior, carrying the sample information as they
 132 scatter back towards the spectrometer. As opposed to traditional OCT systems, the off-axis
 133 BADF-OCT system incorporates an additional channel dedicated to the recovery of scattered
 134 photons. The mean-square heterodyne signal current at the photodetector can be expressed
 135 using the mutual interference function Γ , as follows³⁵:

$$136 \quad \langle i^2(z) \rangle = 2\alpha^2 |g(\tau)|^2 \times \text{Re} \left[\iint \Gamma_S(\mathbf{p}_1, \mathbf{p}_2, z) \Gamma_R(\mathbf{p}_1, \mathbf{p}_2; z) d\mathbf{p}_1 d\mathbf{p}_2 \right], \quad (1)$$

137 where α is a factor that converts power into current, \mathbf{p}_1 and \mathbf{p}_2 are two-dimensional
 138 (2D) vectors transverse to the optical axis, and the subscripts R and S refer to the
 139 reference and sample arms, respectively. In addition, $|g(\tau)|$ is the modulus of the
 140 normalised temporal coherence function of the source, which has a value of 1 when the
 141 sample and reference arm path lengths are matched, and
 142 $\Gamma_{R,S}(\mathbf{p}_1, \mathbf{p}_2; z) = \langle U_{R,S}(\mathbf{p}_1; z) U_{R,S}^*(\mathbf{p}_2; z) \rangle$. Because the incident light fields for both the
 143 reference and sample arms are Gaussian in form, the expressions are as follows:

$$144 \quad U_R(\mathbf{p}, t) = \sqrt{\frac{P_R}{\pi w_0^2}} \exp \left[-\frac{p^2}{2} \left(\frac{1}{w_0^2} + \frac{ik}{f} \right) \right] \cdot \exp[i\omega_R t + \varphi_R(t)] \quad (2)$$

$$145 \quad U_S(\mathbf{p}, t) = \sqrt{\frac{P_S}{\pi w_0^2}} \exp \left[-\frac{p^2}{2} \left(\frac{1}{w_0^2} + \frac{ik}{f} \right) \right] \cdot \exp[i\omega_S t]. \quad (3)$$

146 As the sample arm is incident off-axis onto the focusing lens, the expression for its light
 147 field should be multiplied by the corresponding phase delay $U_S = U_{Si}(\mathbf{p}, t) \cdot e^{i\varphi(\mathbf{p}, z)}$. When
 148 carrying sample information back to the spectrometer, it must pass through both bright- and
 149 dark-field recovery paths according to the following expression:

$$150 \quad U_{SDAB}(\mathbf{p}; z) = U_{Sdark}(\mathbf{p}; z) + U_{Sbright}(\mathbf{p}; z) \\
 = \left(\int_{r_{dark \min}}^{r_{dark \max}} U_B(\mathbf{r}; z) G(\mathbf{r}, \mathbf{p}; z) d\mathbf{r} + \int_{r_{bright \min}}^{r_{bright \max}} U_B(\mathbf{r}; z) G(\mathbf{r}, \mathbf{p}; z) d\mathbf{r} \right) \cdot e^{i\varphi(\mathbf{p}, z)}, \quad (4)$$

151 where $U_{BDAB}(\mathbf{p}; z)$ is the total reflected sample field in the plane of the tissue
 152 discontinuity and \mathbf{r} , \mathbf{r}_1 , and \mathbf{r}_2 are 2D vectors in the plane transverse to the optical axis.

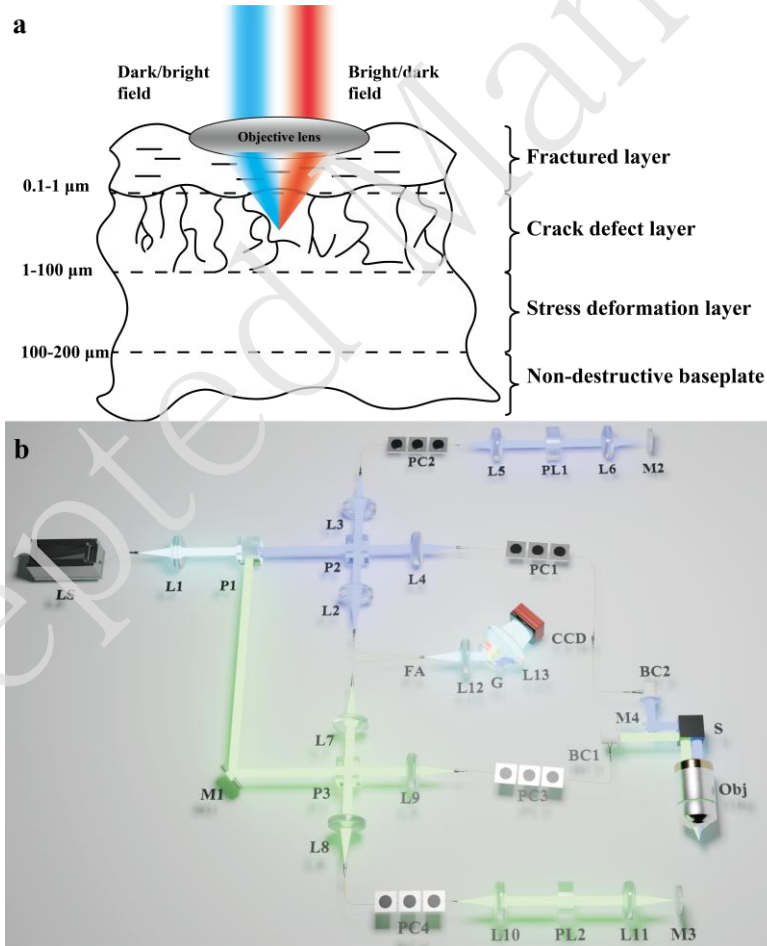
153 $G(\mathbf{r}, \mathbf{p}; z)$ is the extended Huygens–Fresnel Greens function response at \mathbf{p} owing to a

154 point source at \mathbf{r} , which includes the effects of scattering in the intervening medium.

155 The bright and dark fields each have reference arms that interfere with them, and their total
156 mean-square difference signal currents can be expressed as

$$\begin{aligned}
 \langle i^2(z) \rangle_{total} &= \langle i^2(z) \rangle_{dark} + \langle i^2(z) \rangle_{bright} \\
 157 \quad &= 2\alpha_{dark}^2 |g_{dark}(\tau)|^2 \times \text{Re} \left[\iint \Gamma_{Sdark}(\mathbf{p}_1, \mathbf{p}_2, z) \Gamma_{Rdark}(\mathbf{p}_1, \mathbf{p}_2, z) d\mathbf{p}_1 d\mathbf{p}_2 \right] \\
 &+ 2\alpha_{bright}^2 |g_{bright}(\tau)|^2 \times \text{Re} \left[\iint \Gamma_{Sbright}(\mathbf{p}_1, \mathbf{p}_2, z) \Gamma_{Rbright}(\mathbf{p}_1, \mathbf{p}_2, z) d\mathbf{p}_1 d\mathbf{p}_2 \right]
 \end{aligned} \quad (5)$$

158 where $\langle i^2(z) \rangle_{dark}$ and $\langle i^2(z) \rangle_{bright}$ refer to the mean-square heterodyne signal current
159 dark and bright fields, respectively. If necessary, the optical path difference between the
160 reference and sample arms in the bright- and dark-field modes requires an additional distance
161 to enable simultaneous observation at different depths, and $|g(\tau)|$ is divided into distinct
162 values for the bright- and dark-field modes. Similarly, double cameras of the dark and bright
163 fields have different values of α . The principle of the off-axis BADF-OCT detecting SSDs is
164 illustrated in **Fig. 1 a**.



165

166 **Fig. 1 a** Principle of detecting SSDs in SiC using the off-axis BADF-OCT. **b** Schematic of
167 the off-axis synchronous BADF-OCT system. LS: light source; L1–L13: lenses; P1–P3: beam
168 splitters; M1–M4: mirrors; PC1–PC4: polarisation controllers; PL1–PL2: dispersion
169 compensation elements; FA: fibre array; G: grating; CCD: camera; BC1–BC2: reflective

170 beam collimators; S: scanner; Obj: objective lens; blue beam: composite colour light; green
171 beam: bright field; purple beam: dark field.

172 2.2 Optical System and Experimental Methodology

173 The overall structure of the off-axis BADF-OCT is depicted in **Fig. 1 b**. A broad-spectrum
174 light source (SuperK FIANIUM OCT, NKT Photonics) outputs light waves that pass through
175 the beam splitter coupling unit P1. L1 is the collimating lens. To ensure deep penetration of
176 the SiC sample, the system employs a filtered light source with a wavelength range selected
177 within the near-infrared band of 1.1–1.5 μm . The green beam represents the actual
178 illumination beam and the purple beam represents the actual dark field. The illumination
179 beam is divided by P3 into the reference arm and collected by focal lens L8, while the other
180 part is collected by L9 into the sample arm. PC3 is used to control the beam polarisation. The
181 beam after controlled polarisation is collimated by a reflective beam collimator that does not
182 introduce chromatic aberrations. Using scanner S, the beam is focused using an objective lens.
183 When reflected from the samples, the light field photons return along the original route and
184 interfere with the reference photons at P3. Information is collected by lens L7 and sent to the
185 spectrometer. Dark-field photons with scattered angles return along the purple beam route and
186 interfere with the dark-field photons returning from M2 at P2. Simultaneously with the
187 bright-field interference information, dark-field interference information is captured by the
188 spectrometer. Owing to the special structure of the off-axis BADF-OCT system, the purple
189 beam route can also be considered a bright field, and the green beam route can be regarded as
190 a dark field. The spectrometer consists of a collimator, grating, and camera. The working
191 wavelength ranges from 1.1 to 1.5 μm .

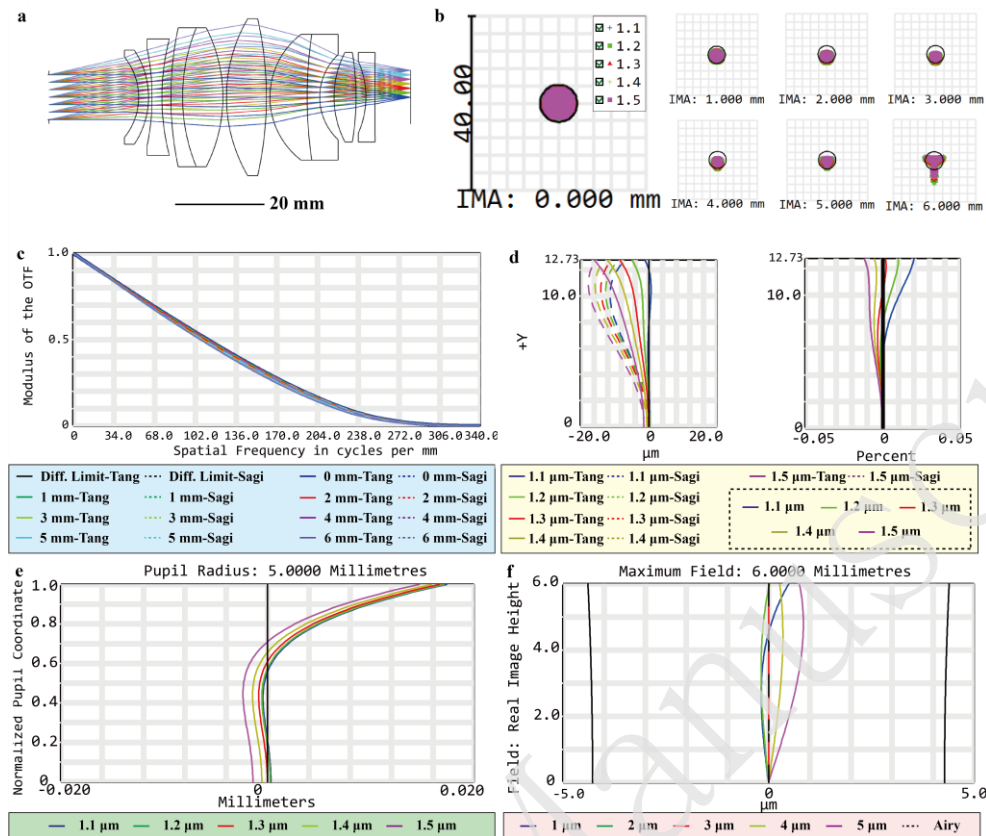
192 In addition, when the green beam acts as a bright field, the purple beam depicted in the
193 figure represents the alignment-guiding beam of the dark-field optical path. Following
194 collimation, it is intentionally injected with a radial offset from the entrance pupil centre of
195 the telecentric scan lens, symmetrically opposite to the radial displacement of the illumination
196 beam, so that it is focused on the sample volume, thereby establishing an additional optical
197 signal channel. A portion of the reflected light field generated at the illuminated sample
198 travels back along the original path of the illumination beam, forming the bright-field signal.
199 Another portion is returned along the guided beam path, corresponding to the region outside
200 the illumination axis and forming the dark-field signal. Although the dark-field guiding beam
201 generates the same illumination and corresponding two-way backlight collection, by
202 introducing a fixed optical path difference to the guiding optical path through the optical path
203 design and combining it with the optical path adjustment function of the bright-/dark-field
204 reference arm, a dynamically adjustable dual Michelson structure synchronous low-coherence
205 interferometric sampling system is constructed, thereby clearly distinguishing the bright- and
206 dark-field signals. In addition, the "coherence gate" effect resulting from the short coherence
207 length is used to isolate the "illumination effect" of the guiding beam naturally, so that the
208 interference signal received by the spectrometer is only the bright-field interference signal
209 and the dark-field interference signal obtained under the single-path illumination condition.

210 In this system, a fibre array spectrometer is specifically designed to acquire
211 bright/dark-field interference signals synchronously²⁶. Employing a conventional illumination
212 lens–grating–lens configuration, this spectrometer utilises two ports in the fibre array to
213 transmit bright- and dark-field interference signals separately, thereby enabling the

214 dual-channel synchronous detection of both interference signals. To provide sufficient optical
215 path adjustment space for the bright- and dark-field signals, two 2048-pixel high-speed linear
216 array detectors (XEN-000688, Xenics) are used to sample the 1100–1500 nm spectral band
217 (with a 0.1 nm spectral sampling rate), achieving an axial sampling range of up to 4.2 mm.
218 The depth corresponding to each pixel is approximately 2 μm . After resampling, the depth of
219 each pixel is 0.54 μm . Combined with the calibration of the scanning galvanometer system,
220 the entire system operates at a frequency of 80–100 kHz, with a sampling SNR of 92 dB.

221 **2.3 Optical Design of Off-Axis BADF-OCT Objective Lens**

222 We propose an optical design of a high-resolution objective lens for the off-axis
223 BADF-OCT system to achieve SSD detection in SiC. Its operating wavelength range is
224 1100–1500 nm, with a centre wavelength of 1300 nm. The layout of the objective lens, which
225 consists of nine spherical lenses, is shown in **Fig. 2 a**. The total length of the objective lens is
226 81 mm. The diameter of the scanning area is 12 mm. The size of the point array in each field
227 of view is shown in **Fig. 2 b**, and the specific values are listed in **Table 1**. The black circles
228 represent the size of the airy spot in the current field of view. The size of the light spot in
229 almost all fields of view is close to the diffraction limit. In **Fig. 2 c**, the transfer functions of
230 all fields are very close to the diffraction limit. As shown in **Fig. 2 d**, the astigmatism in the
231 largest field of view is maintained within 20 μm , and the maximum distortion is
232 approximately 0.02%. The longitudinal aberration is within 20 μm . Considering the working
233 band with a 400 nm bandwidth, two double-glued lenses are included in the system to
234 eliminate chromatic aberration. The vertical chromatic aberration is also well controlled
235 within the range of the airy spot. The longitudinal and vertical chromatic aberrations are
236 shown in **Fig. 2 e** and **f**, respectively. The designed entrance pupil space of this objective lens
237 is 10 mm, with a numerical aperture of 0.185. The object-side full-aperture collection angle is
238 approximately 10.5°. For simultaneous sampling in the bright and dark fields under off-axis
239 illumination, it can be configured to achieve an off-axis collection angle of approximately 5°.



240

241 **Fig. 2** Optical design parameters and performance of off-axis BADF-OCT high-resolution
 242 objective lens. **a** Layout of the objective lens. **b** Size of the spot diagrams for each field of
 243 view. 1.1–1.5: wavelength, 1.1–1.5 μm ; IMA: field of view. The black circle represents the
 244 airy spot size. **c** Transfer functions for each field of view. Diff. limit: diffraction limit; Tang:
 245 tangential; Sagi: sagittal; **d** +Y: line field of view in the Y-direction. The left panel shows the
 246 field curves. The right-hand side shows the distortion. **e** Longitudinal aberration. **f** Lateral
 247 colour.

248

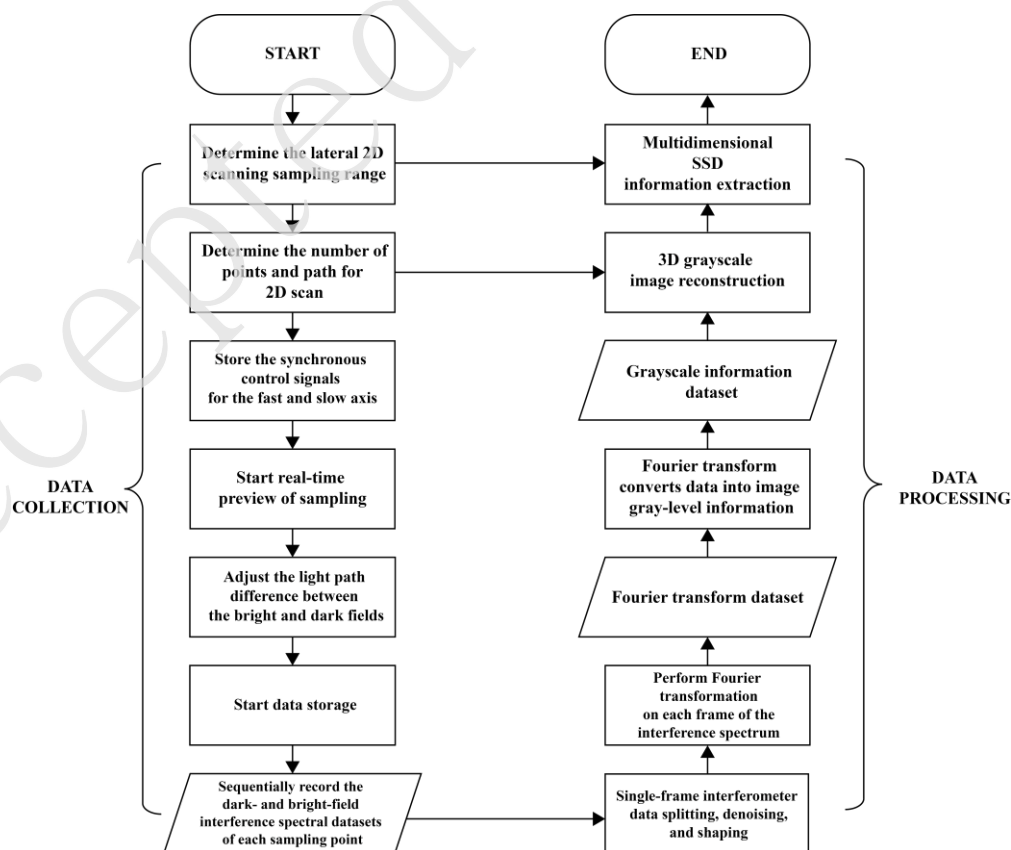
Table 1. Spot size of line field.

Field of view (mm)	0	1	2	3	4	5	6
RMS size (μm)	1.698	1.677	1.651	1.673	1.717	1.730	2.365
GEO size (μm)	3.271	3.963	4.432	4.713	4.792	4.452	11.371

249 2.4 Data Acquisition and Processing Workflow

250 The SSD detection process for SiC is an extension of the OCT image-acquisition method.
 251 In the off-axis BADF-OCT system, the bright- and dark-field dual channels can be
 252 synchronously imaged in the spectrometer when each has a reference arm. The basic
 253 workflow for detecting SSDs in SiC using the off-axis BADF-OCT system is illustrated in
 254 **Fig. 3**. During data acquisition, the sampling range and number of sampling points are first
 255 determined to generate the step voltage signal waveform that controls the deflection of the 2D
 256 galvo mirrors. Within the synchronised timing sequence of the signal generator card, the 2D

257 mirror is steered to scan the beam along the intended path. During the dwell period at each
 258 sampling point, the spectral detector is triggered to expose and capture the interferometric
 259 spectrum. Real-time imaging preview via the control software allows for monitoring of the
 260 bright- and dark-field image acquisition. Adjusting the optical path difference between the
 261 bright- and dark-field modes ensures clear, non-overlapping tomographic images.
 262 Subsequently, the data storage function is activated to record the bright- and
 263 dark-field-synchronised interferometric spectral data from each sampling point sequentially in
 264 a dataset file. Data processing runs concurrently with the acquisition. First, the interferometric
 265 spectrum dataset is segmented into sequential single-frame spectra based on temporal tags.
 266 Spectral shaping is performed after denoising. The series of interferometric spectra then
 267 undergoes Fourier transform processing, with the results stored as a Fourier transform dataset.
 268 The Fourier-transformed interferometric spectral data are further converted into greyscale
 269 information. Based on the pre-defined 2D sampling point count and path established during
 270 data acquisition, the corresponding data from the greyscale information dataset are extracted
 271 to reconstruct a 3D greyscale image. By combining this with the preset 2D scanning sampling
 272 range information, the spatial location, size, and morphological characteristics of the SSD are
 273 extracted from the 3D greyscale image, completing the SSD detection process. Owing to the
 274 processing flow of this algorithm and the characteristics of objects that cause detection
 275 interference, such as dust and water marks on optical elements, which occupy a small surface
 276 area and emit weakly scattered return light, the signals are significantly weaker than those of
 277 smoother surfaces. Meanwhile, the light signals penetrating beneath the surface are amplified,
 278 thereby enhancing the SNR for SSDs. This method of suppressing chaotic surface signals
 279 while amplifying subsurface signals enables the morphology of SSDs to be distinguished
 280 from the interference caused by surface dust.



282 **Fig. 3** Data collection and processing flow. The data acquisition component enables the
283 simultaneous collection of bright- and dark-field signals, with synchronised preview and
284 separate storage. During data processing, subsurface signals are amplified, whereas weak
285 surface stray signals are attenuated, allowing for the reconstruction of 3D structural data for
286 SSDs.

287 3. Results

288 3.1 Spatial and Axial Resolution Testing

289 After completing the experimental system setup, we measured the lateral resolution, depth
290 of focus, axial resolution, and imaging depth of the system for the experimental samples. This
291 process validated the advantages of the dark-field synchronous scheme in terms of the SNR
292 and detection of low-reflectance or weakly scattering targets. **Fig. 4 a** shows a photograph of
293 the constructed off-axis BADF-OCT system. **b** shows the positions of the scanner, objective
294 lens, and sample.

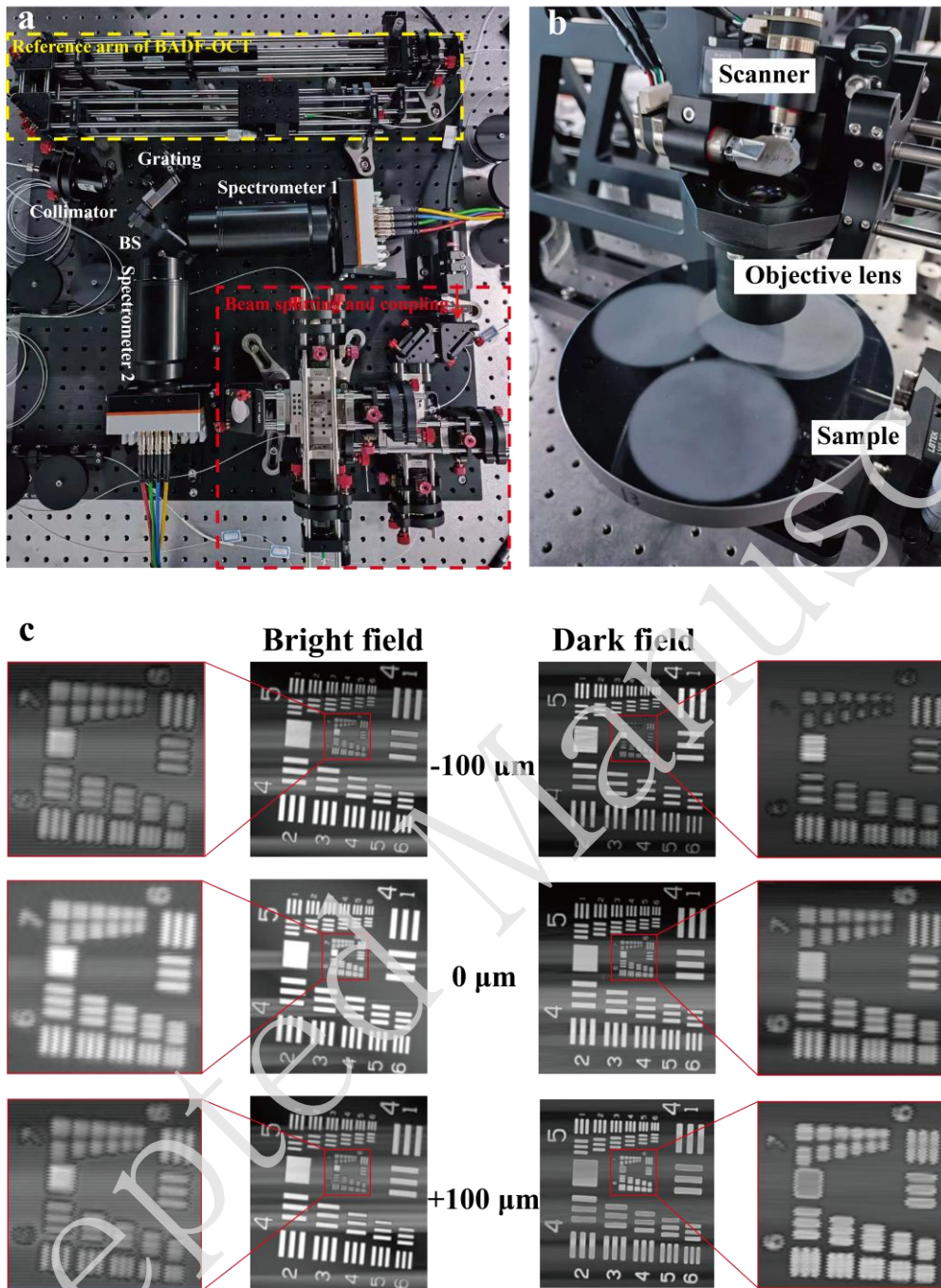
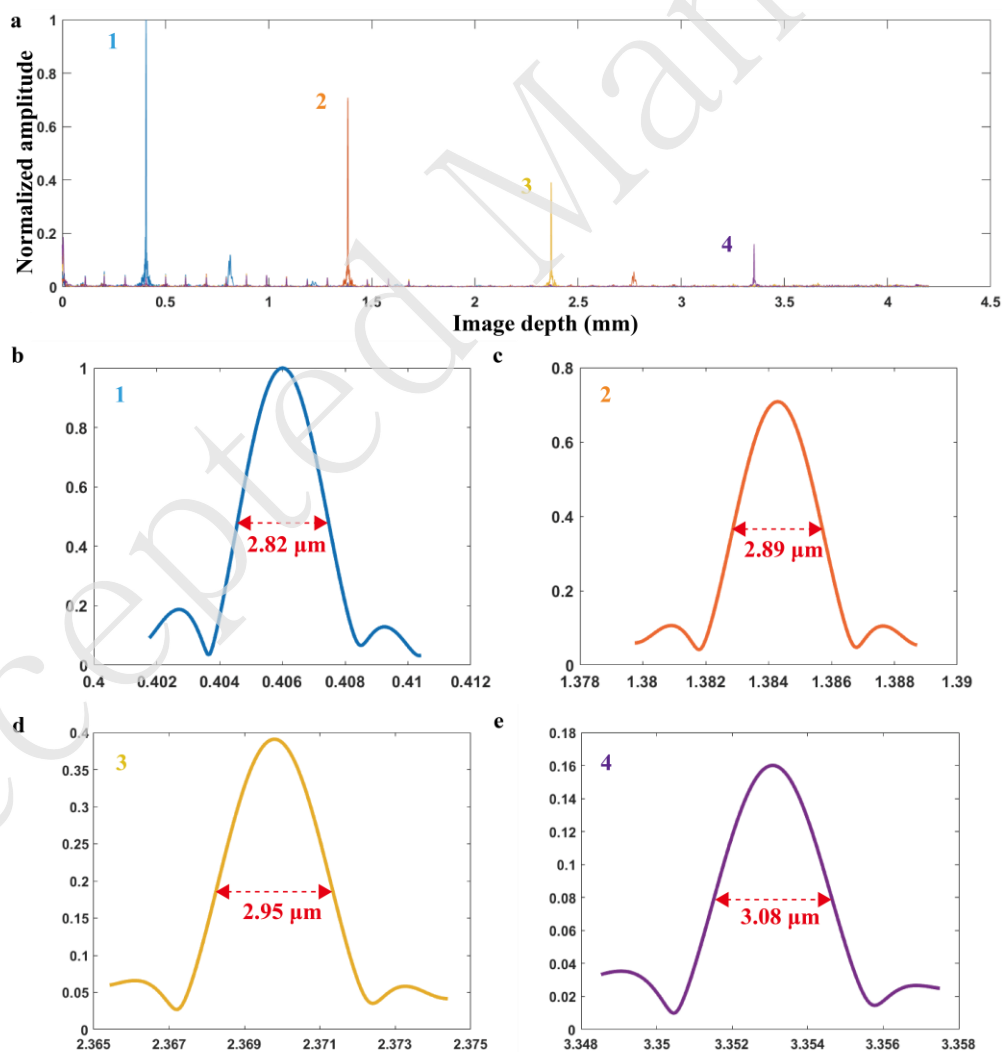


Fig. 4 **a** Images of the off-axis BADF-OCT system. BS: beam splitter. **b** Structure of scanner, objective lens, and samples. **c** Scanning imaging and regions of interest (ROIs) of USAF 1951 resolution board at -100, 0, and 100 μm .

Because the bright and dark fields share the same microscope objective, the light beams for their dual-path illumination occupy only half of the entrance pupil. Therefore, the lateral resolutions and detection depths of these two methods vary. Thus, we imaged the resolution plate and divided it into two parts, namely the bright and dark fields, to test their lateral resolutions separately and obtain the actual spatial resolution. **Fig. 4 c** shows the lateral resolution and depth of the field test results for the bright- and dark-field imaging. The bright- and dark-field imaging results were extracted by directly scanning the USAF 1951 resolution test chart. The images revealed the ability to resolve the 80.61 p/mm pattern in the 6th group,

307 3rd row, indicating a lateral resolution of $12.4\ \mu\text{m}$ for the scanning field lens in air, which was
 308 close to the theoretical calculation. Simultaneously, comparing the imaging effects at ± 100
 309 μm defocus positions from the resolution chart demonstrated that the scanning field lens
 310 depth of field met the theoretical expectations.

311 To ensure lateral resolution and a large imaging depth simultaneously, we constructed a
 312 spectrometer suitable for wavelengths ranging from 1.1 to $1.5\ \mu\text{m}$. A roll-off experiment was
 313 conducted to verify the axial resolution of the system. **Fig. 5** shows the axial resolution test
 314 results for the off-axis BADF-OCT system. A sample arm return beam was generated by
 315 placing a mirror on the focal plane of the scanning field lens of the sample arm. Four
 316 interference spectra corresponding to the different optical path differences were obtained by
 317 progressively increasing the displacement of the reference arm. Following the Fourier
 318 transformation, four point spread functions (PSFs) were obtained, representing imaging
 319 depths ranging from shallow to deep. The results show that the average full width at half
 320 maximum (FWHM) of the diffusion function across four positions from shallow to deep was
 321 $2.935\ \mu\text{m}$, closely approximating the theoretical calculation. The sequential increase in the
 322 FWHM from the shallow to deep points resulted from the combined effects of incomplete
 323 dispersion compensation and the sampling response of the spectrometer.



324
 325

Fig. 5 a Axial PSF at different depths within the measurement range of the off-axis

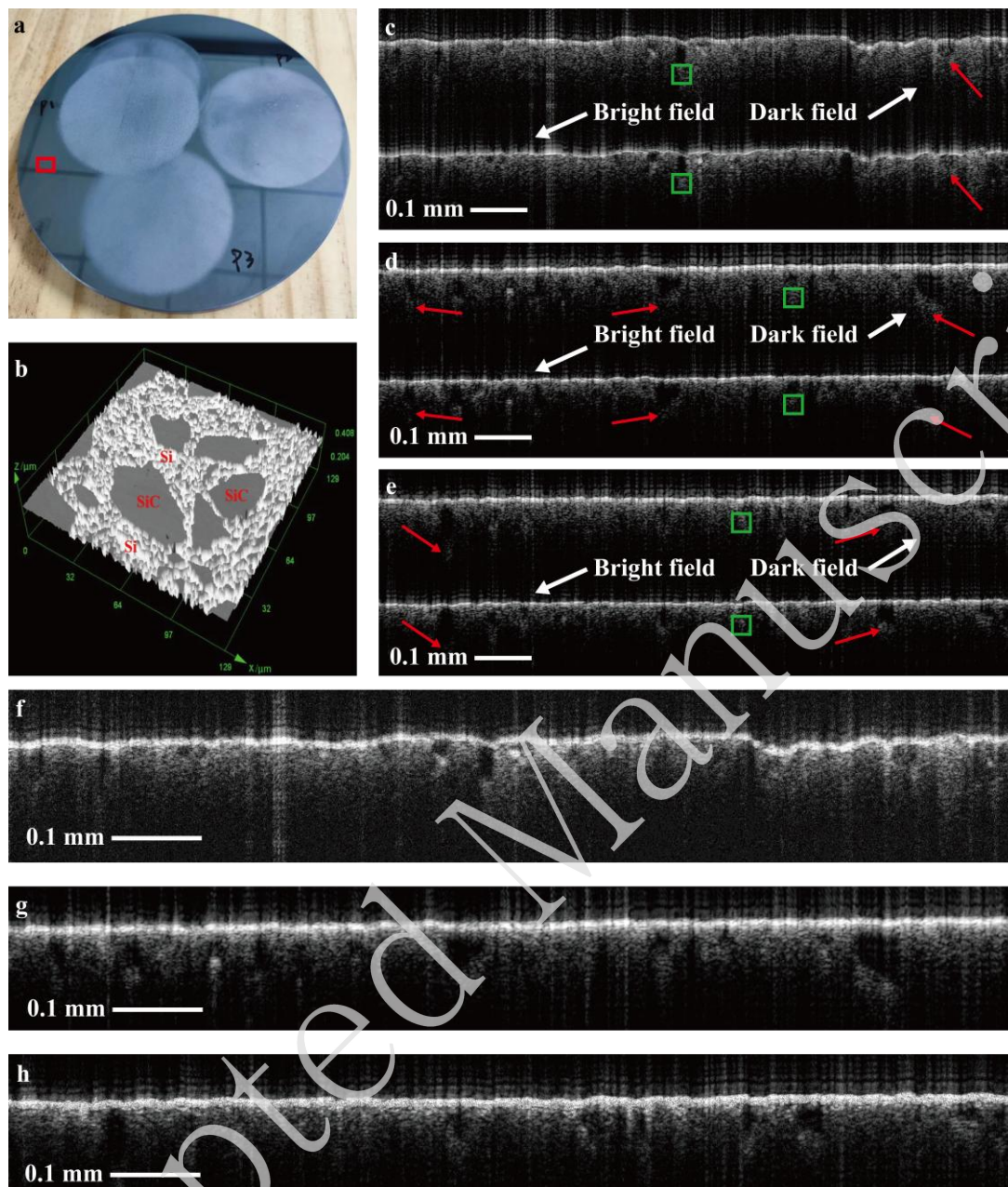
326 BADF-OCT system. **b** Relative peak height at the topmost point of the image, with an
327 FWHM of 2.82 μm . The relative amplitude was 1. **c** 1/3 of image depth, with an FWHM of
328 2.89 μm . The relative amplitude was 0.72. **d** 2/3 of image depth, with an FWHM of 2.95 μm .
329 The relative amplitude was 0.39. **e** Bottom of image depth, with an FWHM of 3.08 μm . The
330 relative amplitude was 0.162.

331 Based on the measured performance of the axial resolution, lateral resolution, and depth of
332 focus in air, the system can achieve chromatographic imaging with an axial resolution better
333 than 1.5 μm and a lateral resolution better than 5 μm within a depth range of approximately
334 30 μm for SiC sample analysis. In addition, the constructed system effectively enhances the
335 resistance to stray light interference by employing off-axis illumination, a broad-spectrum
336 light source, and a fibre array spectrometer solution. Specifically, the off-axis illumination
337 suppresses strong specular reflection interference from the sample surface; the near-infrared
338 broad operating spectrum ensures a high coherent contrast even in environments with intense
339 stray light, demonstrating exceptional environmental adaptability; and the fibre array
340 spectrometer achieves effective spatial filtering by emitting light waves through the fibre end
341 face. The system achieved a measured SNR of 92 dB while maintaining strong resistance to
342 stray light interference, demonstrating robust weak signal detection capabilities. This renders
343 it highly suitable for SSD detection in highly scattering materials.

344 3.2 BADF B-scan Imaging of RB-SiC

345 The test specimens were fabricated from reaction-sintered SiC (RB-SiC), which is a
346 two-phase composite ceramic material formed by infiltrating liquid silicon into SiC (primarily
347 6H-SiC) and carbon powder, followed by sintering. **Fig. 6 a** shows a photograph of the
348 experimental specimen. To ensure that the surface roughness and SSD of the RB-SiC
349 specimen in the experimental testing were entirely generated by the grinding process, the
350 surface was first polished using a cerium oxide polishing solution (with a polishing particle
351 size of approximately 1.5 μm) to achieve a surface roughness of $S_a \approx 15$ nm. At this stage, the
352 SSDs were considered negligible and unlikely to influence subsequent SSD generation during
353 grinding. All three regions (P1, P2, and P3) of the test specimen were ground using an
354 RB-SiC grinding disc matching the specimen material, combined with a diamond
355 micro-powder abrasive at 300 rpm. By setting different grinding pressures (P1: 2 psi, P2: 1
356 psi, and P3: 0.5 psi), progressively reduced roughness was obtained across the three regions
357 (P1: $R_a = 700$ nm, P2: $R_a = 630$ nm, and P3: $R_a = 590$ nm). The surface morphology of the
358 polished RB-SiC captured by the confocal microscope is shown in **Fig. 6 b**, where the dark
359 particles represent the SiC phase and the light substrate constitutes the Si phase. The SiC
360 particles predominantly ranged between 2–10 and 20–40 μm . The Si phase acted as a
361 “binder” between the SiC particles. The interface between the Si and SiC phases is a
362 relatively weak area that may fracture during grinding, causing the SiC particles to detach.
363 The detachment of large SiC particles results in a rougher surface than that of materials such
364 as fused quartz or single-crystal silicon following grinding.

365



366

367

368

369

370

371

372

373

374

375

376

377

378

379

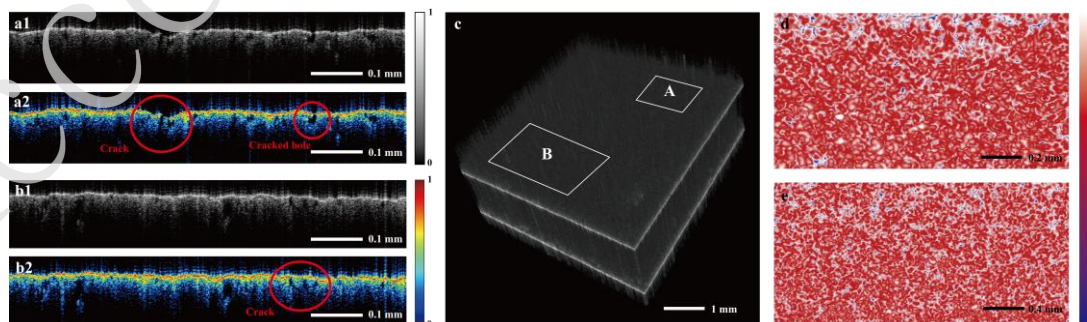
Fig. 6 **a** RB-SiC grinding experimental samples. The red square represents the ROI. **b** Image of ROI. **c**, **d**, and **e** show the synchronised bright- and dark-field tomographic images of P1, P2, and P3, respectively. The green box indicates the ROI used to calculate the CNR. The red arrows represent the differences between the bright and dark fields. **f** P1 image after merging the bright and dark fields. **g** P2 image after merging the bright and dark fields. **h** P3 image after merging the bright and dark fields.

The tomographic penetration effects measured in regions P1, P2, and P3 using the off-axis BADF-OCT system are shown in **Fig. 6 c, d, and e**. As indicated by the red arrow, the dark fields provided deeper information and exhibited better uniformity in the image intensity at greater depths. Notably, the smoother the surface, the brighter the surface in the picture. That is, the rougher the surface, the smaller the difference in signal strength between the surface and depth of the image. The contrast-to-noise ratio (CNR) of the dark-field ROI in P1 was

380 1.07, whereas that of the bright-field ROI was 1.01. In P2, the CNR of the dark-field ROI was
 381 0.7 and that of the bright-field ROI was 0.44. In P3, the CNR of the dark-field ROI was
 382 0.85, and that of the bright-field ROI was 0.61. In addition, the imaging results demonstrate
 383 that for RB-SiC materials, OCT tomographic images can reveal the distribution state of the
 384 SiC and Si phases within the material (large grey areas in the tomographic greyscale images
 385 represent the Si phase, whereas black shadows indicate the SiC phase). Under near-infrared
 386 light in the 1100–1500 nm spectral range, the average imaging depth for the dark-field mode
 387 (115 μm) was greater than that for the bright-field mode (102 μm). In addition, as shown in
 388 **Fig. 6 f, g, and h**, after merging the bright- and dark-field images, the morphology of the SiC
 389 was averaged in the bright- and dark-field images, avoiding the strong light interference of the
 390 bright field and noise of the dark field. Moreover, the advantages of dark-field imaging, that is,
 391 greater depth and superior image contrast, were effectively preserved. These preliminary
 392 experimental results between the confocal microscope and off-axis BADF-OCT system
 393 provide valid proof for SSD detection in RB-SiC.

394 3.3 SSD Imaging

395 Based on the results presented in Section 3.2, we conducted experiments on the SSD of
 396 RB-SiC. The fundamental morphological features of SSDs extend from near-surface locations
 397 to depths of several hundred micrometres. Although SiC particles are also present in this
 398 region and may be confused with scratches and SSDs, the surface-layer SiC exhibits a smooth
 399 surface and high reflectivity after polishing. If surface cracks exist, fractures will appear on
 400 the surface. In particular, in OCT systems, although the surface signal is angle dependent, the
 401 surface intensity in the B-scan image remains relatively uniform following angle adjustment.
 402 **Fig. 7 a1, a2, b1 and b2** show dark-field tomography images of two locations with significant
 403 SSDs in region P1 of the sample. The imaging results demonstrate that the greyscale image
 404 obtained by directly mapping the sampled information from the OCT system exhibited high
 405 contrast. It clearly revealed the rough surface of the ground RB-SiC material and subsurface
 406 structural information within a certain depth range. Building on this, applying
 407 pseudo-colouring processing with reference to the image greyscale values will enable more
 408 accurate identification of surface interface locations and provide a more pronounced
 409 representation of the defect morphology. In addition to revealing SSD information through
 410 axial tomographic images, SSD details can also be visualised by extracting lateral
 411 cross-sectional views of different regions from the 3D greyscale data of the inspection results.



412
 413 **Fig. 7** Tomographic image of the measured SSD position in the P1 region. **a1, b1** Greyscale.
 414 **a2, b2** Colour mapping. **c** Greyscale data cube and horizontal cross-sectional view at a
 415 sampling position in the P3 region. **d** Colour mapping of area A. **e** Colour mapping of area B.
 416 White represents the highest intensity level, blue indicates the lowest intensity level, and red

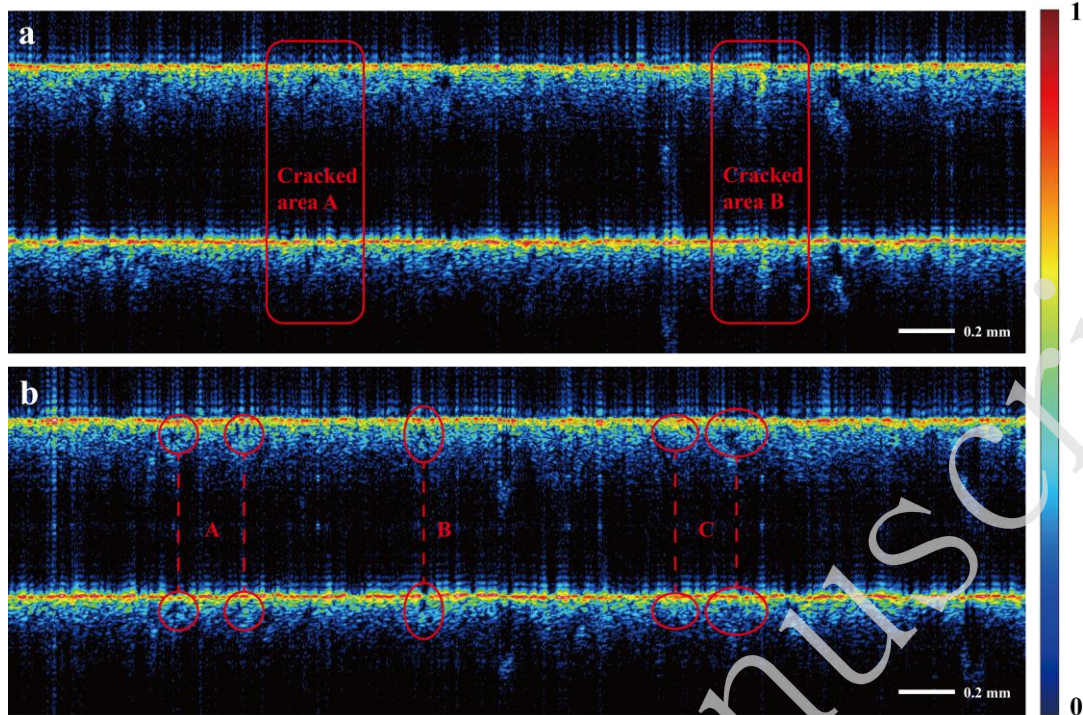
417 signifies a medium-intensity signal.

418

419 For large-scale SSDs, a B-scan image is sufficient for observation. However, for
420 small-scale SSDs, observation using B-scan images is difficult because of the limitations in
421 the number of sampling points and resolution. Thus, within the 3D data cube at a sampling
422 location in region P3 of the sample, regions A and B were selected for lateral sectioning, with
423 the cutting depth reaching approximately 20 μm below the surface, as shown in **Fig. 7 c, d,**
424 **and e.** Because typical SSDs in SiC are cracks that diffuse into deeper layers, the OCT
425 sampling process yielded virtually no scattered signals within the corresponding crack regions.
426 Consequently, the greyscale values in these areas were predominantly zero. By leveraging this
427 greyscale distribution characteristic, pseudo-colour processing of the lateral profile greyscale
428 image (as shown in colour images a and b) visually revealed the lateral distribution of the
429 SSDs. (The fragmented dark blue areas in the image indicate the SSD locations.) In summary,
430 the digital profiling method based on OCT sampling data enables the efficient and convenient
431 extraction and analysis of SSD information in SiC.

432 **3.4 Multi-angle Imaging of SSD Based on Dual-Path BADF Acquisition**

433 As this system adopts a dual-path coordination mechanism, both paths simultaneously
434 perform the functions of bright-field illumination and dark-field collection, thereby generating
435 two angles of bright- and dark-field synchronous imaging. This observation method provides
436 a more comprehensive imaging of the SSDs. During the detection of SSDs using the off-axis
437 BADF-OCT system, it was observed that the SSD information reflected by the bright- and
438 dark-field sampling signals did not consistently exhibit high consistency, as shown in **Fig. 8 a**
439 (dark-field signal above, bright-field signal below). Instead, certain sampling positions
440 exhibited differences, as illustrated in **Fig. 8 b.** For instance, region A exhibited differing
441 defect morphologies at identical sampling locations, region B showed variations in the axial
442 defect positions, and region C displayed defect information in dark-field signals but lacked
443 clear defect indications in bright-field signals. The analysis indicated that this issue stems
444 from multiple refractive-index discontinuities within the crack region, coupled with complex
445 scattering characteristics. The differing optical paths during bright- and dark-field signal
446 collection lead to signal instability, ultimately manifesting as discrepancies in the imaging
447 results. Synchronous bright- and dark-field imaging and fusion analysis effectively mitigate
448 the detection uncertainties inherent in single-mode OCT imaging, enabling precise defect
449 localisation and enhancing the defect detection rates and accuracy. Furthermore, through
450 intensity analysis of the SiC tomographic images, the sample surface with the maximum and
451 most stable signal distribution could be clearly distinguished from the defect layer exhibiting
452 random signal fluctuations. Utilising the 3D information from stable signal peak points
453 enables the extraction of surface topography data, whereas signal distribution differences
454 provide a basis for defect classification. Combined with the fusion analysis of bright- and
455 dark-field signal distribution variations, this approach can further enhance the accuracy of
456 surface topography detection and defect classification.



457

458

459

460

461

462

Fig. 8 a In the simultaneous imaging of bright- and dark-fields, although at different positions of the same sample, due to the differences in the illumination of the beam and the collection angle of photons, there are two forms of SSD image morphology: similarity and difference. The marked cracked areas A and B represent the similarity of SSD. **b** Differences in bright- and dark-field synchronised tomographic image.

463

4. Discussion and Conclusions

464

465

466

467

468

469

470

471

472

473

474

475

476

477

478

479

480

481

482

This study has addressed the challenges of SSD detection in SiC components, particularly RB-SiC, during processing, in which traditional inspection methods are either destructive or inefficient. A non-destructive testing method based on an off-axis BADF-OCT system was proposed. The system integrates a broadband light source, fibre array spectrometer, and off-axis illumination/detection configuration to achieve high-resolution imaging with lateral resolution better than 5 μm and axial resolution better than 1.5 μm . It also offers advantages such as a large depth of field, strong anti-interference capability, and high SNR. The experimental results demonstrate that this method not only effectively distinguishes between surface fracture layers and subsurface crack layers, but also enhances defect detection rates and classification accuracy through the synergistic bright-/dark-field mechanism. Compared with existing methods, this system exhibits comprehensive advantages in terms of non-destructive testing, resolution, detection depth, and defect type discrimination. It provides a viable pathway for the quality control of SiC optical components and lays the foundation for expanding OCT technology applications in industrial inspection.

Owing to the highly complex morphology of SSDs, despite our experimental success in distinguishing the structures from those of SiC phases, industrial and intelligent defect identification remains indispensable. In future work, we will develop high-precision, high-speed SSD recognition algorithms based on the off-axis BADF-OCT system to provide stronger technical support for non-destructive SSD detection in SiC.

483 **Acknowledgements**

484 This research was supported by the Jilin Province Science and Technology Development
485 Project (SKL202502022JC); Jilin Science and Technology Development Plan (No.
486 20240101029JJ); Synchronized high-speed detection of surface shape and defects in the
487 grinding stage of complex surfaces (KLMSZZ202305); High precision wide dynamic large
488 aperture optical inspection system for fine astronomical observation: National Major
489 Research Instrument Development Project (62127901); Ultra-smooth manufacturing
490 technology of large diameter complex curved surface: National Key R&D Program
491 (2022YFB3403405); and Research on the key technology of rapid synchronous detection of
492 surface shape and subsurface defects in the grinding stage of large diameter complex surface:
493 International Cooperation Project (2025010157). This study was also supported by the Key
494 Laboratory of Optical System Advanced Manufacturing Technology, Chinese Academy of
495 Sciences (2022KLOMT02-04).

496 **Author Contributions**

497 **Dacheng Wang:** Experiment, data analysis. **Chengchen Zhou:** Writing. **Yukun Wang:**
498 Concept, Review & editing. **Lingzhong Li:** Experiment. **Yue Ding:** Data curation. **Zhongkai**
499 **Liu:** Editing. **Nanguang Chen:** Supervision. **Linbo Liu:** Data collection. **Xiaokun Wang:**
500 Supervision & principle. **Donglin Xue:** Supervision. **Xuejun Zhang:** Supervision.

501 **Data Availability**

502 All data required to evaluate the conclusions of this study are presented in the paper and/or
503 Supplementary Materials. Additional data related to this paper may be requested from the
504 authors.

505 **Conflicts of Interest**

506 The authors declare that they have no known competing financial interests or personal
507 relationships that could have appeared to influence the work reported in this paper.

508 **References**

- 509 1. Zhong, B. et al. Process chain for ultra-precision and high-efficiency
510 manufacturing of large-aperture silicon carbide aspheric mirrors. *Micromachines*
511 **14**, 737 (2023) doi: 10.3390/mi14040737
- 512 2. Miyasaka, Y., Kondo, K. & Kiriya, H. High-thermal-conductivity SiC ceramic
513 mirror for high-average-power laser system. *Crystals* **10**, 831 (2020) doi:
514 10.3390/cryst10090831
- 515 3. Chen, B. Q. et al. SiC diffractive waveguides for augmented reality: single-layer,
516 full-color, rainbow-artifact-free display with vision correction. *eLight* **5**, 21 (2025)
517 doi: 10.1186/s43593-025-00100-1
- 518 4. Zhang, X. J. et al. Challenges and strategies in high-accuracy manufacturing of
519 the world's largest SiC aspheric mirror. *Light: Science & Applications* **11**, 310
520 (2022) doi: 10.1038/s41377-022-00994-3
- 521 5. Yan, Y. H. et al. High-precision laser slicing of silicon carbide using temporally
522 shaped ultrafast pulses. *Light: Advanced Manufacturing* **6**, 65 (2025) doi:
523 10.37188/lam.2025.065

- 524 6. Rao, X. S. et al. Surface and subsurface damage of reaction-bonded silicon
525 carbide induced by electrical discharge diamond grinding. *International Journal of*
526 *Machine Tools and Manufacture* **154**, 103564 (2020) doi:
527 10.1016/j.ijmachtools.2020.103564
- 528 7. Xie, X. Z. et al. Low-damage precision slicing of SiC by simultaneous dual-beam
529 laser-driven crack expansion of silicon carbide. *Optics & Laser Technology* **192**,
530 113960 (2025) doi: 10.1016/j.optlastec.2025.113960
- 531 8. Liu, C. L. et al. Cutting mechanism of reaction-bonded silicon carbide in
532 laser-assisted ultra-precision machining. *International Journal of Machine Tools*
533 *and Manufacture* **203**, 104219 (2024) doi: 10.1016/j.ijmachtools.2024.104219
- 534 9. Ganguly, N., Sopeña, P. & Grojo, D. Ultra-high-aspect-ratio structures through
535 silicon using infrared laser pulses focused with axicon-lens doublets. *Light:*
536 *Advanced Manufacturing* **5**, 22 (2024) doi: 10.37188/lam.2024.022
- 537 10. Karci, Ö. & Beldek, T. B. Quantitative investigation of abrasive grit size
538 dependency of subsurface damages for the metal-bonded abrasives on Zerodur
539 glass-ceramic. *Applied Optics* **60**, 2624-2632 (2021) doi: 10.1364/ao.419820
- 540 11. Esmailzare, A., Rahimi, A. & Rezaei, S. M. Investigation of subsurface damages
541 and surface roughness in grinding process of Zerodur® glass-ceramic. *Applied*
542 *Surface Science* **313**, 67-75 (2014) doi: 10.1016/j.apsusc.2014.05.137
- 543 12. Grundmann, J. et al. Optical and tactile measurements on SiC sample defects.
544 *Journal of Sensors and Sensor Systems* **13**, 109-121 (2024) doi:
545 10.5194/jsss-13-109-2024
- 546 13. Quan, H. D., Shi, W. Q. & Kong, L. B. Non-destructive optical measurement of
547 transparent objects: a review. *Light: Advanced Manufacturing* **6**, 22 (2025) doi:
548 10.37188/lam.2025.022
- 549 14. Brinksmeier, E. State-of-the-art of non-destructive measurement of sub-surface
550 material properties and damages. *Precision Engineering* **11**, 211-224 (1989) doi:
551 10.1016/0141-6359(89)90031-7
- 552 15. Fine, K. R. et al. Non-destructive real-time direct measurement of subsurface
553 damage. Proceedings of SPIE 5799, Modeling, Simulation, and Verification of
554 Space-Based Systems II. Orlando, Florida, United States: SPIE, 2005. doi:
555 10.1117/12.602993
- 556 16. Tian, A. L. et al. A novel method for subsurface damage measurement of optical
557 components. *Acta Photonica Sinica* **42**, 214-218 (2013) doi:
558 10.3788/gzxb20134202.0214
- 559 17. Neauport, J. et al. Imaging subsurface damage of grinded fused silica optics by
560 confocal fluorescence microscopy. *Optics Express* **17**, 3543-3554 (2009) doi:
561 10.1364/OE.17.003543
- 562 18. Williams, W. et al. Using quantum dots to evaluate subsurface damage depths
563 and formation mechanisms in glass. *CIRP Annals* **59**, 569-572 (2010) doi:
564 10.1016/j.cirp.2010.03.137
- 565 19. Williams, W. B. et al. Using quantum dots to tag subsurface damage in lapped
566 and polished glass samples. *Applied Optics* **48**, 5155-5163 (2009) doi:
567 10.1364/AO.48.005155

- 568 20. Kurniawan, I. S. et al. Nondestructive detection and identification of electrically
569 active threading dislocations in n⁺-SiC substrates. *Nanoscale Advances* **8**,
570 331-339 (2026) doi: 10.1039/D5NA00970G
- 571 21. Huang, D. et al. Optical coherence tomography. *Science* **254**, 1178-1181 (1991)
572 doi: 10.1126/science.1957169
- 573 22. Nie, J. C. et al. Method for extracting optical element information using optical
574 coherence tomography. *Sensors* **24**, 6953 (2024) doi: 10.3390/s24216953
- 575 23. Xu, Z. Y. et al. Dual beam optical coherence tomography angiography for
576 decoupling axial velocity gradient. *Scientific Reports* **14**, 19464 (2024) doi:
577 10.1038/s41598-024-68924-4
- 578 24. Matveev, L. A. et al. Online platform for generating realistic digital phantoms of
579 OCT signals and performing multimodal processing towards optical cancer
580 diagnostics. *Light: Advanced Manufacturing* **6**, 6 (2026) doi:
581 10.37188/lam.2026.006
- 582 25. Zhou, C. C. et al. Dynamic needle beam design and intensity uniformity
583 optimization for enhanced optical coherence tomography using liquid crystal
584 spatial light modulator. *Optics & Laser Technology* **195**, 114582 (2026) doi:
585 10.1016/j.optlastec.2025.114582
- 586 26. Wang, Y. K. et al. Multi-channel spectral-domain optical coherence tomography
587 using single spectrometer. *Chinese Optics Letters* **21**, 051102 (2023) doi:
588 10.3788/col202321.051102
- 589 27. Zhuo, Y. M. et al. Retinal thermal deformations measured with phase-sensitive
590 optical coherence tomography in vivo. *Light: Science & Applications* **14**, 151
591 (2025) doi: 10.1038/s41377-025-01798-x
- 592 28. Zvagelsky, R. et al. Towards *in-situ* diagnostics of multi-photon 3D laser printing
593 using optical coherence tomography. *Light: Advanced Manufacturing* **3**, 39 (2022)
594 doi: 10.37188/lam.2022.039
- 595 29. Hasegawa, S. et al. In-process monitoring in laser grooving with line-shaped
596 femtosecond pulses using optical coherence tomography. *Light: Advanced*
597 *Manufacturing* **3**, 33 (2022) doi: 10.37188/lam.2022.033
- 598 30. Hu, Y. Z. & Gao, W. R. Detecting subsurface damage within glasses with
599 polarization-sensitive optical coherence tomography. *Optics & Laser Technology*
600 **177**, 111146 (2024) doi: 10.1016/j.optlastec.2024.111146
- 601 31. Israelsen, N. M. et al. Real-time high-resolution mid-infrared optical coherence
602 tomography. *Light: Science & Applications* **8**, 11 (2019) doi:
603 10.1038/s41377-019-0122-5
- 604 32. Rao, D. S. S. et al. Shot-noise limited, supercontinuum-based optical coherence
605 tomography. *Light: Science & Applications* **10**, 133 (2021) doi:
606 10.1038/s41377-021-00574-x
- 607 33. Zhao, Y. et al. Dual-axis optical coherence tomography for deep tissue imaging.
608 *Optics Letters* **42**, 2302-2305 (2017) doi: 10.1364/ol.42.002302
- 609 34. Matthews, T. E. et al. Deep tissue imaging using spectroscopic analysis of
610 multiply scattered light. *Optica* **1**, 105-111 (2014) doi: 10.1364/optica.1.000105
- 611 35. Untracht, G. R. et al. Spatially offset optical coherence tomography: leveraging

612 multiple scattering for high-contrast imaging at depth in turbid media. *Science*
613 *Advances* **9**, eadh5435 (2023) doi: 10.1126/sciadv.adh5435

Accepted Manuscript